Journal of Statistical Mechanics: Theory and Experiment
An IOP and SISSA journal

Failure as a critical phenomenon in a progressive damage model

L Girard[1], **D Amitrano**[2] **and J Weiss**[1]

[1] Laboratoire de Glaciologie et Géophysique de l'Environnement, CNRS—Université Joseph Fourier, Grenoble, France
[2] Laboratoire de Géophysique Interne et de Tectonophysique, CNRS—Université Joseph Fourier, Grenoble, France
E-mail: lgirard@lgge.obs.ujf-grenoble.fr, david.amitrano@ujf-grenoble.fr and weiss@lgge.obs.ujf-grenoble.fr

Received 4 September 2009
Accepted 7 December 2009
Published 21 January 2010

Online at stacks.iop.org/JSTAT/2010/P01013
doi:10.1088/1742-5468/2010/01/P01013

Abstract. The critical point hypothesis for fracture is tested using a progressive damage model. The advantage of the present model, based on continuum mechanics, is the possibility of tracking the approach to final failure in terms either of discrete events (the avalanches) or of the resulting continuous strain field. Different but actually closely linked phenomena are reported. In terms of damage avalanches, power law distributions of avalanche sizes and energies are observed associated with a finite size scaling. The finite size scaling is also observed for the spatial correlations of damage events. A divergence of the correlation length is reported in the vicinity of final failure, from a correlation analysis of discrete events and from a scaling analysis of the continuous strain rate field. We also show that multifractal properties of the deformation emerge from the long-range elastic interactions that occur near final failure. All of these results argue for a critical point interpretation of failure. Finally, we discuss the implications of our results for the criticality of fracture and deformation of geophysical objects, and for associated precursory phenomena.

Keywords: correlation functions (theory), finite-size scaling, avalanches (theory), fracture (theory)

1742-5468/10/P01013+28$30.00

Contents

1. Introduction

Fracture is a multiscale phenomenon, from the scale of individual crystals (μm to mm) to the scale of plate tectonics or of the Arctic sea ice cover (beyond 10^3 km). Predicting the failure of a sample, a structure, or a geophysical object is a long-standing problem of fundamental importance in engineering and in geophysics (e.g. tentatively predicting earthquakes). In the classical Griffiths theory of brittle fracture in a pure crystal [1], disorder is absent within the material except a single flaw whose size and geometry dictate the failure strength. In this case, upon increasing the applied stress (or strain), predicting the failure in a deterministic sense is impossible, except if one knows exactly the characteristics of the flaw, as failure occurs suddenly without precursors. If one draws an analogy with phase transitions, this transition to failure is of first order [2, 3]. However, disorder is inherent in any real material and its role as regards fracture and strength has been stressed for a long time [4]. The classical approach for dealing with this problem is purely statistical, considers a population of flaws within the material with various sizes and characteristics, and assumes that the failure of the whole structure is dictated by the activation of the most dangerous (generally the largest) flaw. This weakest-link approach assumes that defects are non-interacting, and have no effect on the propagation of a crack once nucleated. This approximation seems reasonable in the case of a structure with weak disorder (i.e. the local, 'microscopic' strength is narrowly distributed), under loading conditions that do not stabilize crack propagation (e.g. monotonic tension).

J. Stat. Mech. (2010) P01013

In the case of stronger disorder and/or loading conditions under which crack propagation is more stable (e.g. compression, shear), the situation is different. For the last few years, there has been growing evidence, either experimental or from statistical models, that 'macroscopic' failure can be preceded, or actually presaged, by several precursory phenomena. Fracture in heterogeneous media is considered to be an example of 'crackling noise', i.e. the system responds to slow externally applied driving through discrete, impulsive events spanning a broad range of sizes [5]. Experimentally, the most powerful non-destructive technique for recording this crackling noise is that of acoustic emission (AE). Power law distributions of AE energies, $P(E) \sim E^{-\beta}$, have been observed for various loading conditions and materials [6]–[11], taking into account all the events recorded throughout the test. However, fracture at the laboratory scale under monotonic loading is characterized by a lack of time invariance, i.e. the activity strongly increases on approaching final failure (defined as the maximum sustainable stress σ_c). A decreasing β has been reported to accompany this increasing activity, that is, larger events become relatively more frequent, for laboratory experiments as for the collapse of rocky cliffs and, more controversially, for earthquakes or volcanoes [8, 11, 12].

This evolution can also be tracked via an increase of the integrated energy release rate δE. This increase can result from an increase of the average event size, as noted above, and/or from an increasing event rate [6]. Under strain rate control, this energy release rate has been observed to increase exponentially before failure [9, 13], whereas there is some evidence of a power law divergence under stress control $\delta E \sim [(\sigma_c - \sigma)/\sigma_c]^{\kappa}$ [13] (under these conditions, this can be equivalently expressed as a function of time, $\delta E \sim (t_c - t)^{\kappa}$). Such behavior has been reported for constant load conditions, that is, creep [8, 14, 15]. The approach to failure can also be tracked in the spatial domain: hypocenters of AE events related to fracture precursors appear to be more and more clustered on approaching failure, and this has been quantified through a decrease of the associated fractal dimension [13], [16]–[19]. These precursory phenomena and associated scaling laws suggest an analogy with critical phenomena, the transition to failure becoming in this case a critical 'phase' transition [3]. However, this interpretation is still controversial [2, 20].

To test these ideas, different statistical models of fracture have been developed, with increasing levels of complexity, from the equal load sharing fiber bundle (FBM) model (e.g. [21]), to more sophisticated lattice models such as the random fuse model (RFM) [22] or the more realistic tensorial random spring model (RSM) [2], which both take into account long-range interactions within the media. In all these models, macroscopic failure is preceded by avalanches of local failure events. Power law distributions of avalanche sizes S (defined as the number of broken fibers or bonds) and energies E [20] have been obtained, however with exponents depending on the model considered. Finite size scaling has been reported for these distributions, an argument in favor of a critical interpretation of failure [20, 23].

The evolution of these distributions during the fracture process has also been interpreted as a signature of imminent failure. For the FBM and the RFM, a crossover behavior in the avalanche distribution has been reported, defining two scaling regimes associated with two specific power law exponents and with a crossover scale that diverges on approaching the final failure [20, 24]. Zapperi *et al* [23] showed instead, for the RFM, truncated power laws, $P(S) \sim S^{-\beta} \exp(-S/S_0)$, with an exponential cut-off S_0 diverging towards final failure. In both cases, this divergence of the crossover scale or of the

J. Stat. Mech. (2010) P01013

cut-off means that the average avalanche size is increasing, in qualitative agreement with the increase of the energy release rate observed in experiments. In the spatial domain, a decrease of the correlation dimension of the broken bond patterns has been reported for an antiplane shear loading of a RSM [25] and for a continuous damage model under compression [26, 27], indicating a progressive spatial clustering of fracture events on approaching final failure.

Fracture at the laboratory scale seems therefore to be preceded by several precursory phenomena that can be interpreted in terms of a critical phase transition, and might allow us to predict failure to some extent [3]. Is this framework still relevant at geophysical scales, as is often postulated (e.g. [28]–[30])? This question arises as the fracture of a geophysical object like the Earth's crust is also characterized by scaling laws, such as a power law distribution of earthquake energies [31], or a fractal clustering of hypocenters [32, 33]. In the case of the Arctic sea ice cover, seismic monitoring of fracturing is scarce (see e.g. [34]), but the much faster dynamics allows us to track from satellite imagery directly the evolution through time and space of the deformation field resulting from the multiscale fracturing [35]. These strain fields are characterized by time and space scaling laws that can be theoretically related to the scaling laws describing the space and time clustering of fracture events [36].

However, a fundamental difference exists between these geophysical situations and the fracture at the laboratory scale: the time invariance. Neither the Earth's crust nor the sea ice cover have fallen apart entirely so far. At large time and spatial scales, the system remains in a 'marginally stable' state characterized by apparently stable scaling laws. This might be explained by the presence of healing mechanisms that compensate for the fracturing. Nevertheless, attempts have been made to export the critical point concept, with precursory phenomena, to the Earth's crust at a regional scale, in order to tentatively predict large earthquakes. These approaches were based on a possible divergence of the energy release rate [28, 37], a divergence of the correlation length of earthquake epicenters [38] or a modification of the power law exponent of earthquake energies [39]. Both power law acceleration of energy release and decrease of the power law exponent have been observed before a chalk cliff collapse [8]. Note that in this case the object failed entirely, as in the laboratory model. Despite this notable successful exception, these approaches remain highly controversial, without convincing success so far [40].

In this paper, we test the critical point hypothesis for fracture from a progressive damage model. The continuum mechanics framework allows us to track the approach to failure in terms either of discrete events (the avalanches) or of resulting strain fields. Different but actually closely linked phenomena are reported, which can all be interpreted as a divergence of the correlation length on approaching final failure, therefore arguing for a critical point interpretation of failure. A relationship between the exponents characterizing the avalanche size and energy distributions and the strain field is proposed. The paper is organized as follows. Section 2 describes the progressive damage model and the set of simulations used in this study. Section 3 covers the analysis of the distributions of avalanche size and energy. Spatial correlations of damage are examined in section 4, while the spatial dependence of the strain rate field is considered in section 5. The results are finally discussed in section 6.

J. Stat. Mech. (2010) P01013

2. Numerical modeling

The model that we used is based on progressive isotropic damage that is represented by the reduction of the elastic modulus, reflecting the increase in crack density (see e.g. [41] for the relationship between crack density and effective modulus). Such a framework is in good agreement with the progressive damage observed in brittle materials at the laboratory sample scale [42, 43], particularly when loaded in compression. The effective elastic modulus, Y_{eff}, is expressed as a function of the initial modulus, Y_{ini}, and the damage parameter, $d < 1$:

$$Y_{\text{eff}} = Y_{\text{ini}} d. \tag{1}$$

Such a relationship is valid for a domain which is large compared with the micro-defect size. This supposes that each element is large enough compared with the elementary cracks. In such a case, the damage can be associated with a crack density. The simulated material is discretized in triangular elements using a finite element method with a plane stress hypothesis. The strain and stress fields are considered explicitly as a continuum. The hypothesis of elastic softening applies well under compression as elastic behavior is observed for a wide range of materials with elastic modulus spreading over several orders of magnitude. The loading consists in uniaxial compression, applied by increasing the vertical displacement (strain controlled loading) or force (stress controlled loading) on the upper boundary of the model. The lower boundary of the model is fixed (no displacement) while the left and right boundaries can deform freely, as shown in figure 2(a). In strain driven simulations, the loading increment is extrapolated to damage of the weakest element, whereas in stress driven simulations, a constant increment stress is applied. In both cases, the loading increment ensures a very low driving rate, so stress redistribution during an avalanche happens almost instantaneously, as expected for real materials. This defines a loading step. After each loading step, when the stress of an element, i, exceeds a given strength threshold for damage, its elastic modulus, Y_i, is multiplied by a factor d_0, d_0 being a constant slightly smaller than 1 ($d_0 = 0.9$):

$$Y_i(n+1) = Y_i(n) d_0, \tag{2}$$

n being the number of events of damage of the element i. After n damage events, the effective modulus, $Y_i(n)$ of element i is given by

$$Y_i(n) = Y_{i,0} {d_0}^n \tag{3}$$

where $Y_{i,0}$ is the initial Young's modulus. Because of the elastic interactions, the stress redistribution around a damaged element can induce damage of neighboring elements and set off an avalanche of damaged elements. The avalanche stops when the damage criterion is no longer fulfilled by any element. The damage threshold is calculated using the Mohr–Coulomb criterion, which applies for brittle materials under compressive stress states [44]:

$$\tau = \mu \sigma_{\text{N}} + C \tag{4}$$

where τ is the shear stress, σ_{N} is the normal stress, C is the cohesion and μ is the internal friction coefficient. To simulate material heterogeneity, the value of the cohesion C is randomly drawn from a uniform distribution. C is only drawn once at the beginning of the

J. Stat. Mech. (2010) P01013

simulation (quenched disorder). Redrawing a new cohesion from the initial distribution each time an element is damaged (annealed disorder) does not significantly affect the results. Randomness is necessary to obtain macroscopic behaviors differing from those of the elements and to avoid trivial behavior (failure without precursors at a prescribed strength and simultaneous damage of all elements). Compared to more classical statistical models of fracture, the moduli Y_i and the cohesion C are the equivalents of respectively the spring stiffness (RSM) and the bond breaking threshold [45]. To analyze the influence of material heterogeneity, two series of simulations are performed with different ranges of heterogeneity. For the H_1-range, C is drawn from 5×10^{-4} to $10^{-3} \times Y_{\text{ini}}$, while for the broader H_2-range, C is drawn between 2×10^{-4} and $10^{-3} \times Y_{\text{ini}}$.

A wide range of macroscopic behaviors can be simulated by the model, from brittleness to ductility. This variety of behaviors appears to be controlled by μ which influences the local interaction geometry and therefore controls the ductile–brittle transition [7, 26, 27]. In this study, we use $\mu = 0.7$ which is common to most geomaterials, such as granite, sandstone, limestone [44, 46] and ice [47]. The simulations are performed on rectangular meshes (height to width ratio of 2) of triangular elements. Two sets of meshes are used: 'structured meshes' with similar orientation of all triangles and 'random meshes' with random orientation of triangles. Meshes of linear size L varying from 4 to 128 are used, where the total number of elements is given by $N_{\text{mesh}} = 4L(L-1)$. Extensive statistical sampling was used to obtain the results presented in the following sections. The number of independent simulations performed with each system size is 5000 up to $L = 16$, 3000 for $L = 32$, 500 for $L = 64$ and 20 for $L = 128$. Simulations on structured meshes are only performed with the H_1-range.

The simulations are started with an undamaged material. In the early stage of the simulation, damage is homogeneously scattered throughout the system and the macroscopic behavior of the material is linear. As avalanche activity increases, a deviation from elasticity is observed, corresponding to a softening of the material (figure 1). At this stage, avalanches of all sizes can occur. In strain driven simulations, large avalanches induce a drop in the macroscopic stress and a temporary stabilization of the system. Such relaxation cannot occur in stress driven simulations as stress is continuously increased. Finally, a catastrophic avalanche occurs, spanning from one side of the system to the other (figure 2). In stress driven simulations, the catastrophic avalanche grows indefinitely, as the material cannot hold the imposed stress any longer. Instead, in strain driven simulations, the catastrophic avalanche is followed by a steady state with a macroscopic plastic behavior. In this state, the strain increments are compensated by damage in such a way that the macroscopic stress remains approximately constant [45]. The structured mesh is anisotropic, inducing preferential directions for damage propagation as shown in figure 2. This is not the case for the random mesh, which is isotropic. However, a rigorous analysis of fracture orientation is not within the scope of this study. In what follows, we focus the analysis on the pre-failure state, up to peak load, which we consider as a critical point. The main variables and exponents used in the analysis are presented in table 1.

3. Avalanches

In this section we analyze the distributions of avalanches in terms of size and dissipated energy. We define the avalanche size S as the number of elements damaged during a single

J. Stat. Mech. (2010) P01013

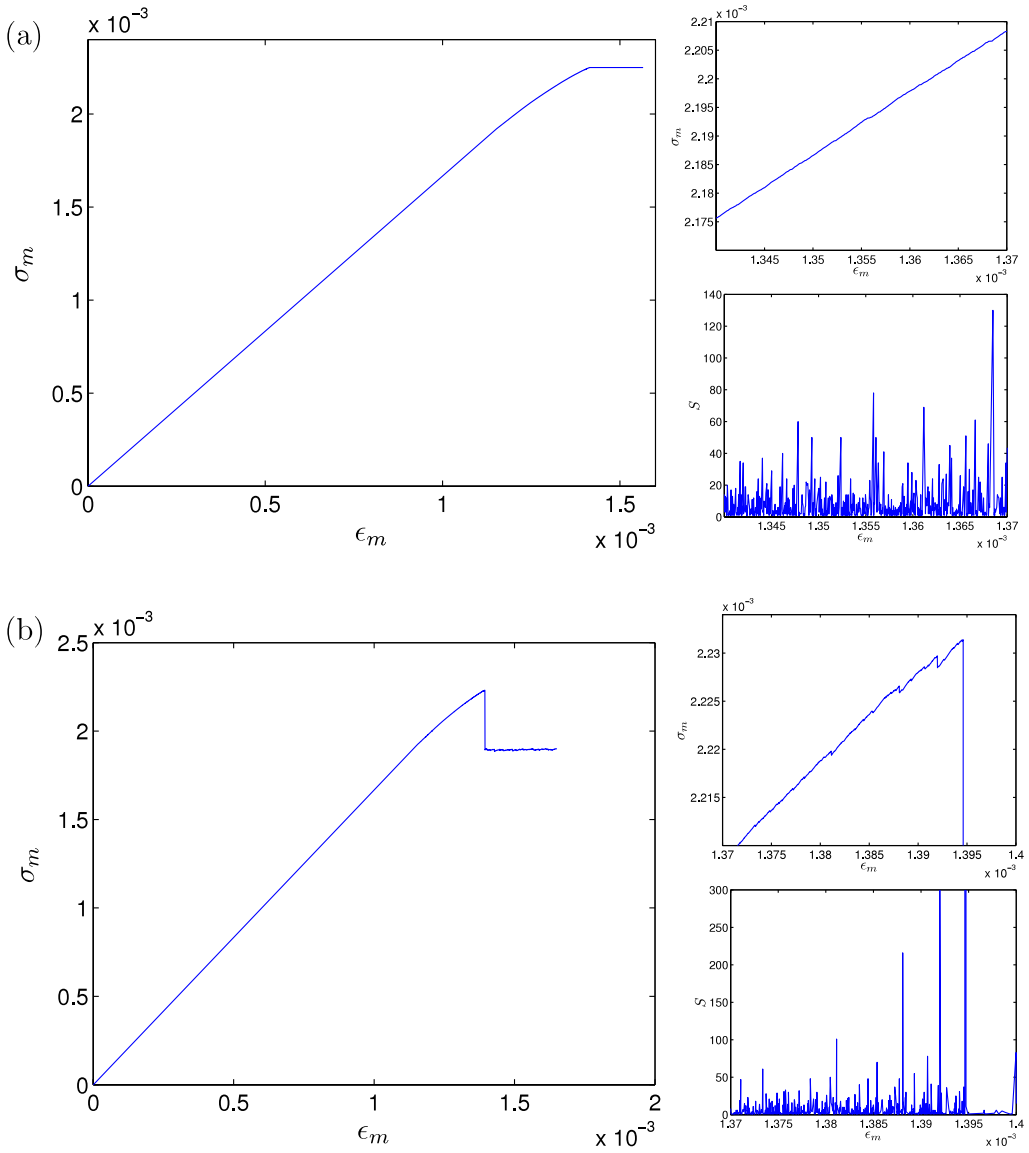

Figure 1. Example of macroscopic strain σ_{m} versus stress ϵ_{m}, for (a) stress controlled simulation and (b) strain controlled simulation. The right panels are zooms of the macroscopic stress/strain curve and the avalanche size S record. σ_{m} is normalized by the Young's modulus.

loading step. In large avalanches, an element can encounter several damage events within a loading step but this is not quantified in S. However, we verified that S scales linearly with the number of damage events, i.e. the effect of multiple damage on one element is minor. Considering elements of equal surface areas, S is proportional to the fault surface area involved in the avalanche. The dissipated elastic energy can be considered as the main contributor to AE and there is strong experimental evidence that AE is a localized phenomenon in space and time, and so energy release occurs at the microfracture scale [13, 16, 48]. We therefore define the dissipated elastic energy E as the sum of the energy losses for every element of the system that was damaged during an avalanche. The

J. Stat. Mech. (2010) P01013

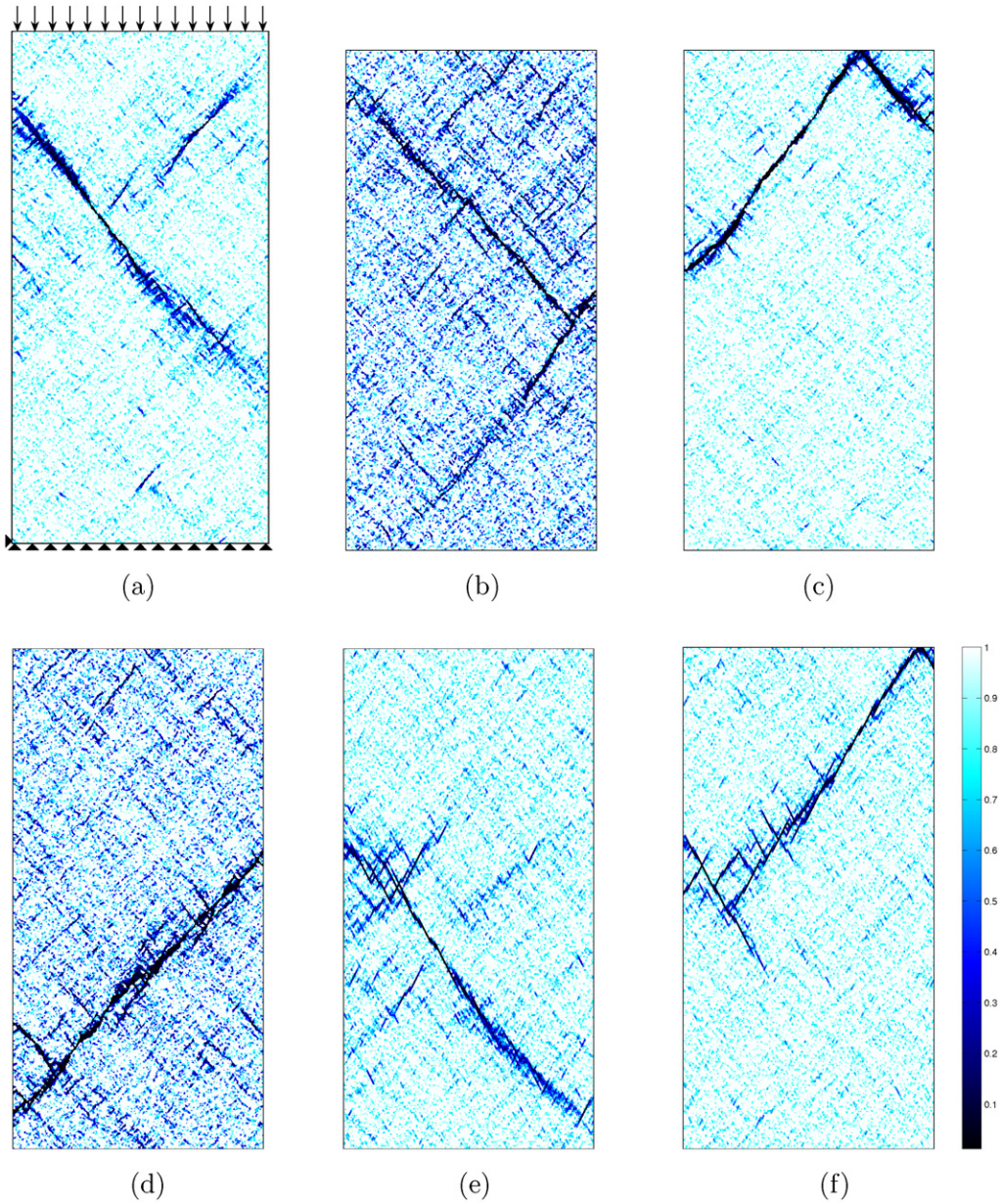

Figure 2. Map of the normalized Young's modulus after the catastrophic avalanche for both mesh types (random, structured), loading modes (stress and strain controlled) and heterogeneity ranges (H_1- and H_2-ranges). (a) rand., stress, H_1, (b) rand., stress, H_2, (c) rand., strain, H_1, (d) rand., strain, H_2, (e) struct., stress, H_1 and (f) struct., strain, H_1.

energy dissipated during the nth avalanche E_n is calculated as

$$E_n = \sum_{\text{damage events}} (1 - d_0) \frac{A_i}{2} \underline{\underline{\sigma}}_i : \underline{\underline{\epsilon}}_i \tag{5}$$

where d_0 is the damage parameter, A_i is the surface area of the ith element, $\underline{\underline{\sigma}}_i$ and $\underline{\underline{\epsilon}}_i$ are respectively the stress and strain tensors of the ith element (before damage), the

Table 1. List of main variables and exponents.

Symbol	
S	Avalanche size
E	Dissipated elastic energy
α, β	Avalanche size/energy distribution exponents
δ	Avalanche size/energy cut-off exponent
γ	Avalanche size/energy critical exponent
D	Correlation dimension
ξ, λ	Correlation length and related critical exponent
η	Cut-off exponent of the correlation length
$\dot{\epsilon}$	Deformation rate
ρ, ν	Scaling and critical exponents of deformation

sum runs over each damage event of the nth avalanche. This definition is equivalent to the *microscopic dissipated energy* defined by Picallo and Lopez [20] for the RFM. The proximity to macroscopic failure is tracked in terms of a control parameter Δ defined as

$$\Delta = \frac{\sigma_{\mathrm{mp}} - \sigma_{\mathrm{m}}}{\sigma_{\mathrm{mp}}}, \qquad \text{for stress driven simulations} \tag{6}$$

$$\Delta = \frac{\epsilon_{\mathrm{mp}} - \epsilon_{\mathrm{m}}}{\epsilon_{\mathrm{mp}}}, \qquad \text{for strain driven simulations} \tag{7}$$

where σ_{m} and ϵ_{m} are respectively the macroscopic stress and strain, reaching values of σ_{mp} and ϵ_{mp} at peak load. The critical point is therefore identified as the peak load. As we are not interested in the linear elastic behavior that precedes the first damage event, σ_{m} and ϵ_{m} are set to zero when the first damage event occurs. The control parameter varies between $\Delta = 1$ at the first damage event and $\Delta = 0$ at the macroscopic failure.

3.1. Finite size scaling

Figure 3 shows the distributions of avalanche sizes S and dissipated energy E for various system sizes, for all damage events up to peak load ($1 \geq \Delta > 0$). The last catastrophic avalanche is out of trend and can thus be considered as an outlier. By analogy with the FBM and RFM, this last avalanche is most likely of significantly different nature than the other avalanches [23], and is not analyzed here. The probability density functions follow a power law with an exponential cut-off at large sizes/energies, sometimes referred to as a gamma law [3]:

$$P(x) \sim x^{-\alpha_x} \exp(-x/x_0) \tag{8}$$

where $x = S$ or E. The cut-off size x_0 increases with the system size L. We make the hypothesis that this cut-off is the expression of a finite size scaling (FSS) and that it scales as $x_0 \sim L^{\delta_x}$. The moment analysis provides a powerful tool for testing these scalings and extracting the exponents α_x and δ_x [49]. We define the q-moment of x on a system size L as $\langle x^q \rangle_L = \int x^q P(x)\,\mathrm{d}x$. If the FSS hypothesis is valid, at least in the asymptotic limit

J. Stat. Mech. (2010) P01013

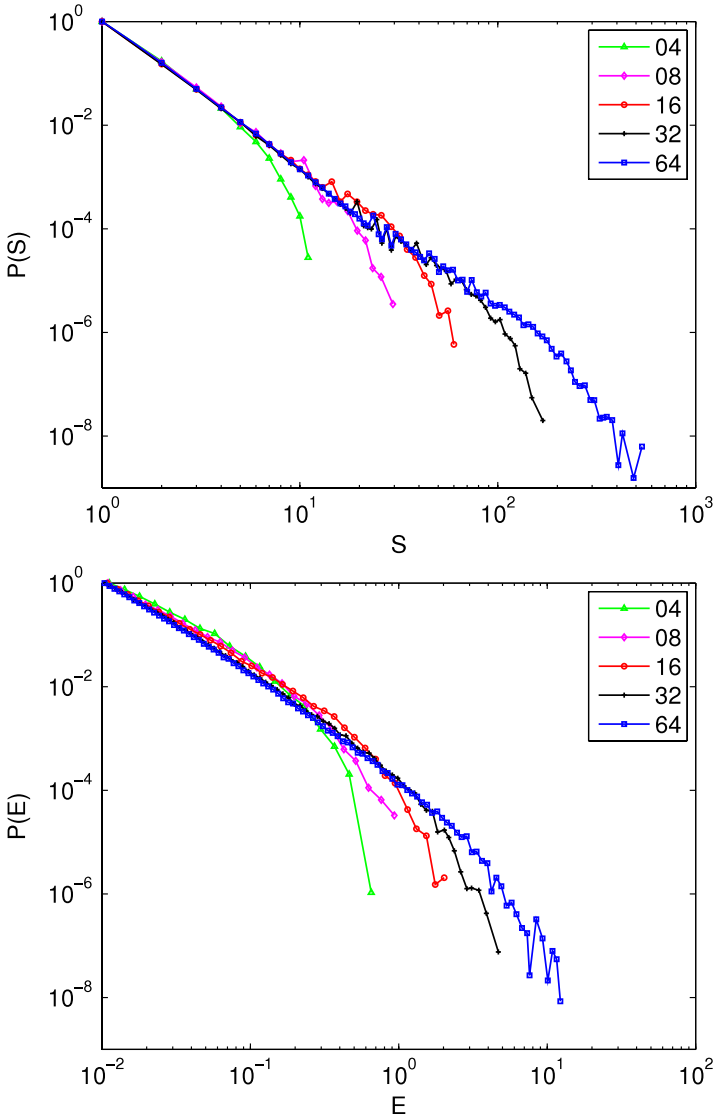

Figure 3. Probability density functions of avalanche size and dissipated energy for the random mesh for strain controlled simulations (H_2-range). Distributions obtained with stress controlled conditions, a regular mesh and/or a narrower range of heterogeneity (H_1) have a similar shape. The functions are normalized by their maximum value.

$(x \to \infty)$, we can make the transformation $z = x/L^{\delta_x}$ and obtain

$$\langle x^q \rangle_L = L^{\delta_x(q+1-\alpha_x)} \int z^{q+\alpha_x} \exp(-z)\, \mathrm{d}z. \tag{9}$$

For $q > \alpha_x - 1$, this can be approximated by $\langle x^q \rangle_L \sim L^{\chi_x(q)}$ where $\chi_x(q) = \delta_x(q + 1 - \alpha_x)$. The exponents $\chi_x(q)$ can be obtained as the slope of the log–log plot of $\langle x^q \rangle_L$ versus L. Figure 4 shows the results obtained from the momentum analysis for $x = S$. As extensive statistical sampling is required to characterize the FSS; the largest system size $L = 128$ is not considered here. $\chi_S(q)$ as a function of q shows a clear linear variation

J. Stat. Mech. (2010) P01013

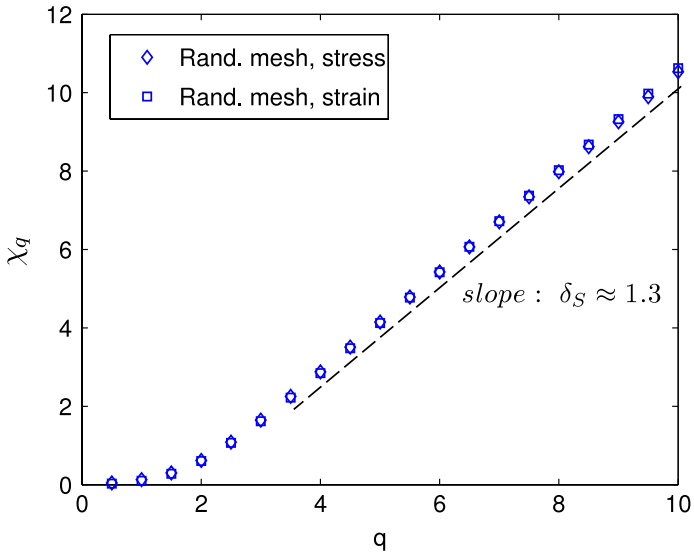

Figure 4. The scaling exponent χ_q of the q th moment of the distribution of avalanche size S for the random mesh and both loading modes (H_2-range). For $q > 3$, a linear fit is applied to χ_q to estimate the values of α_S and δ_S (equation (9)).

starting from $q \approx 3$. For smaller q we observe deviations from the FSS because the integral of equation (9) is dominated by the lower cut-off for small q moments. The linear part of the function $\chi_x(q)$ is used to estimate the exponents δ_x and α_x from the relation $\chi_x(q) = \delta_x(q + 1 - \alpha_x)$; the results are presented in tables 2 and 3. To validate these results we perform a data collapse using the estimated value of the exponents. The representation of $P(x)L^{(\alpha_x-1)\delta_x}$ as a function of x/L^{δ_x} shows a good collapse (figure 5). For a given variable (S or E), the exponents do not significantly vary with the mesh type or the loading mode. The range of material heterogeneity does not have a strong influence on the exponent values. The only significant difference concerns the value of α_E which is slightly lower for the H_2-range than for the H_1-range.

We examine the link between S and E by sorting avalanche sizes and energies in bins and averaging over all realizations of the disorder. We find a clear scaling relationship, $E \sim S^{\omega}$, with $\omega = 1.2 \pm 0.05$ which applies for both loading modes, mesh types and heterogeneity ranges (figure 6). From this, one would expect $\alpha_E = (\alpha_S + \omega - 1)/\omega$ and $\delta_E = \omega\delta_S$. These values are in slight disagreement with the energy exponents reported in tables 2 and 3, especially regarding the cut-off exponent δ_E. These differences could be explained by the uncertainties.

The FSS exponent obtained with the two-dimensional RFM model is in the same range as the results that we obtain for δ_S ($\delta = 1.17$–1.18 [23]). The power law exponents α_S obtained with our model are also in the same range as those obtained with the RFM ($\alpha = 2.75$ with a diamond lattice, and $\alpha = 3.05$ with a triangular lattice [23]), or the RSM ($\alpha \approx 2.6$). This is in turn very close to the mean field value 5/2 obtained in fiber bundle models. Thus, considering the avalanche statistics, the present model (true two-dimensional) does not differ very much from the pseudo-two-dimensional RSM (one-dimensional elements connected in two dimensions) and the one-dimensional RFM.

J. Stat. Mech. (2010) P01013

Table 2. Exponent values for the avalanche distributions, the spatial correlations of damage and the spatial dependence of the strain rate field for the H_1-range.

Loading	Stress		Strain		
Mesh type	Random	Structured	Random	Structured	
α_S	2.7	2.5	2.6	2.6	±0.2
α_E	2.5	2.4	2.5	2.5	±0.2
δ_S	1.2	1.1	1.2	1.3	±0.2
δ_E	1.0	1.0	1.3	1.3	±0.2
β_S	1.8	1.8	1.8	1.8	±0.2
β_E	1.8	1.8	1.9	1.9	±0.2
γ_S	2.0	2.0	2.0	2.0	±0.5
γ_E	2.0	2.0	2.0	2.0	±0.5
D	1.15	1.15	1.15	1.20	±0.05
η	1.1	1.1	1.1	1.2	±0.1
λ	1.0	1.0	1.0	1.0	±0.1
$\rho(1)$	0.15	0.15	0.15	0.16	±0.02
ν	1.0	0.9	1.0	1.0	±0.1

Table 3. Exponent values for the H_2-range.

Loading	Stress	Strain	
α_S	2.6	2.7	±0.2
α_E	2.1	2.1	±0.2
δ_S	1.3	1.4	±0.2
δ_E	1.2	1.2	±0.2
β_S	1.9	1.9	±0.2
β_E	1.9	1.8	±0.2
γ_S	2.0	2.0	±0.5
γ_E	2.0	2.0	±0.5
D	1.3	1.4	±0.1
η	1.1	1.1	±0.1
λ	1.0	1.0	±0.2
$\rho(1)$	0.15	0.15	±0.02
ν	1.0	1.0	±0.1

3.2. Distributions

We now consider the distribution of avalanche sizes and energies for different values of the control parameter Δ. This analysis is done by sorting out avalanches from several realizations of the disorder in log-spaced bins of Δ. We then compute the distribution of each bin (figure 7). The distribution follows a gamma law:

$$P(x, \Delta) \sim x^{-\beta_x} \exp(-x/x^*) \tag{10}$$

where $x = S$ or E. The cut-off size x^* increases with Δ and with the system size L. β_x is estimated such that equation (10) fits the distribution of the bin closest to macroscopic

J. Stat. Mech. (2010) P01013

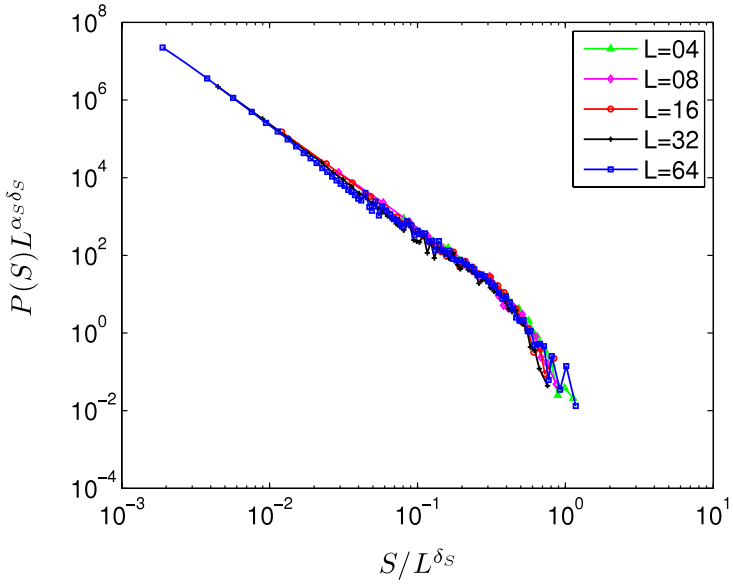

Figure 5. Data collapse of the distributions of avalanche size S for the random mesh under strain control, $\alpha_S = 2.8$ and $\delta_S = 1.3$ (H_2-range).

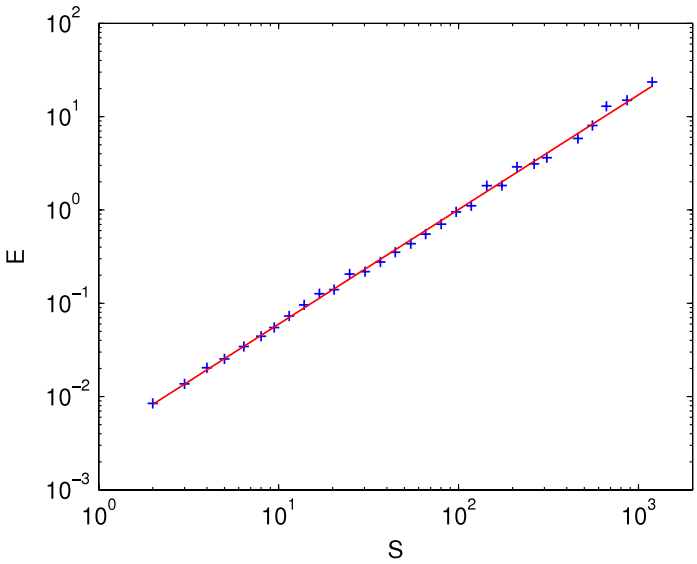

Figure 6. Scaling relationship between the avalanche size S and the dissipated energy E (random mesh under strain control, $L = 64$, H_2-range); the red line is a power law fit, $E \sim S^{1.2}$.

failure (tables 2 and 3). Using the methodology of equation (9), we show that the second moment of the distribution scales as $\langle x^2 \rangle \approx (x^*)^{3-\beta_x}$. Following Zapperi *et al* [23], we assume that for infinitely large systems $x^* \sim \Delta^{-\gamma_x}$, so we can expect the singularity to be rounded at small L as

$$x^* \sim \frac{L^{\delta_x}}{\Delta^{\gamma_x} L^{\delta_x} + c} \tag{11}$$

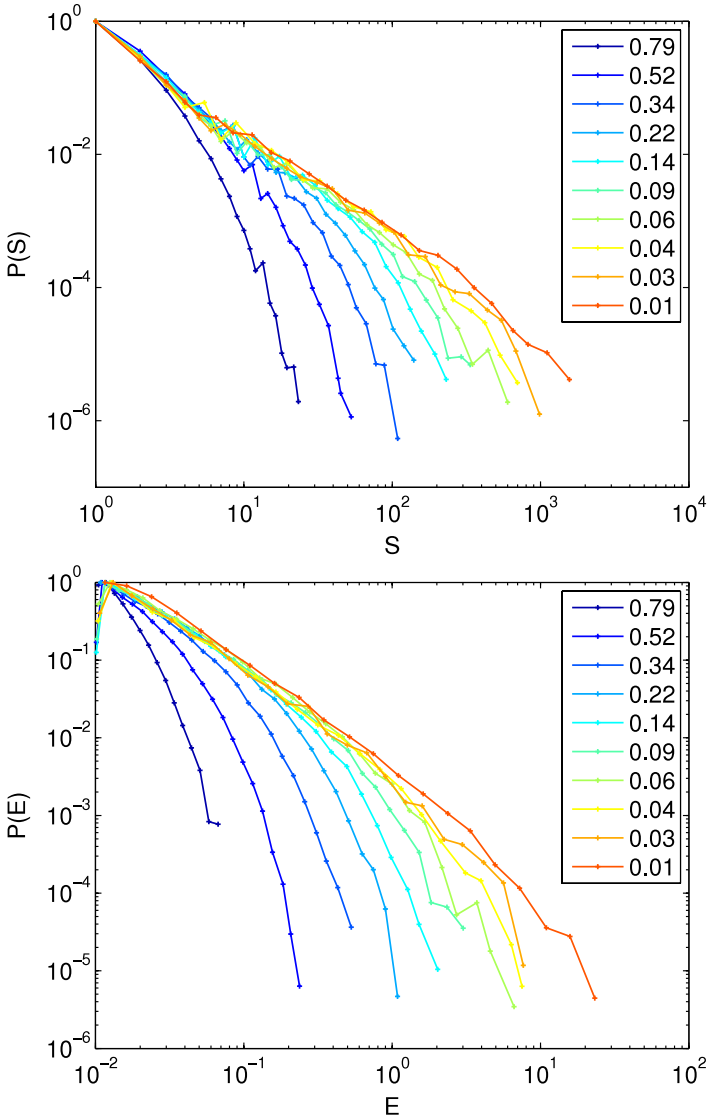

Figure 7. Probability density functions of avalanche size and dissipated energy for different bins of the control parameter, for the random mesh ($L = 128$) under strain control (H_2-range). Distributions obtained with stress controlled conditions, a regular mesh and/or a narrower range of heterogeneity (H_1) have a similar shape. The functions are normalized by their maximum value.

where c is a constant. The value of γ_x is estimated in order to allow the collapse of $\langle x^2 \rangle$ (figure 8).

The exponents for S and E are within the same range. As for α_x and δ_x, one would have expected instead slight differences, owing to the $E \sim S^{\omega}$ scaling. The exponents β and γ do not vary with the type of mesh or the loading mode. The divergence of the maximum avalanche size towards the critical point is the same under stress and strain control. The range of material heterogeneity does not significantly affect this divergence, as the value of γ remains similar for H_1- and H_2-ranges. A detailed comparison of avalanche size and energy distributions shows that the divergence of the

J. Stat. Mech. (2010) P01013

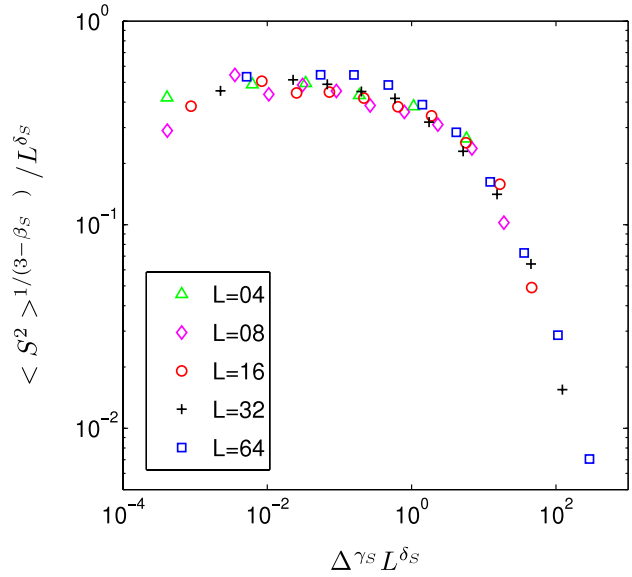

Figure 8. The second moment of the distribution of avalanche size S as a function of the control parameter for the random mesh under strain control can be collapsed using the exponents $\beta_S = 1.9$, $\delta_S = 1.4$ and $\gamma_S = 2.0$ (H_2-range).

largest avalanche is actually slightly less abrupt for the H_2-range. This expresses that a broader heterogeneity range increases the number of precursors. Nevertheless the effect is too small to significantly impact the value of the critical exponent γ_S. In comparison, simulations with the RFM indicated a similar β but a smaller value of γ ($\gamma \approx 1.4$, [23]). This means that the divergence of the maximum avalanche size on approaching final failure is more abrupt in our case.

Integrating equation (10) over Δ, described as sweeping the control parameter towards an instability [3], we obtain the theoretical relation: $\alpha_x = \beta_x + 1/\gamma_x$. This relation is compared to the estimated data. The worst comparison is for the random mesh under stress control (H_1-range), where $\beta_S + 1/\gamma_S = 2.3 \pm 0.5$ while $\alpha_S = 2.7 \pm 0.3$. The comparison improves for the other cases.

3.3. Rate of energy dissipation

Avalanche activity can alternatively be tracked via the evolution of the energy release rate. We define the energy release rate $\mathrm{d}E/\mathrm{d}\Delta$ as the energy dissipated by damage over windows of Δ, normalized by the window width and averaged over different realizations of the disorder. $\mathrm{d}E/\mathrm{d}\Delta$ shows a steep increase at the start of the simulation, bending towards a shallower slope in the vicinity of the macroscopic failure (figure 9). Below $\Delta = 10^{-2}$ the evolution becomes very much fluctuating due to a lack of data.

As $\mathrm{d}E/\mathrm{d}\Delta$ simply scales as the mean dissipated energy $\langle E \rangle$ in our case, we relate its evolution to the distribution of E. This relation arises from an avalanche being triggered at every loading step, with the result that the number of avalanches per window of Δ, normalized by the window width, is constant. The spatial discretization of the numerical model imposes the existence of a lower bound in the distribution of dissipated energy. In the early stage of the simulation, the cut-off term E^* is close to this lower bound.

J. Stat. Mech. (2010) P01013

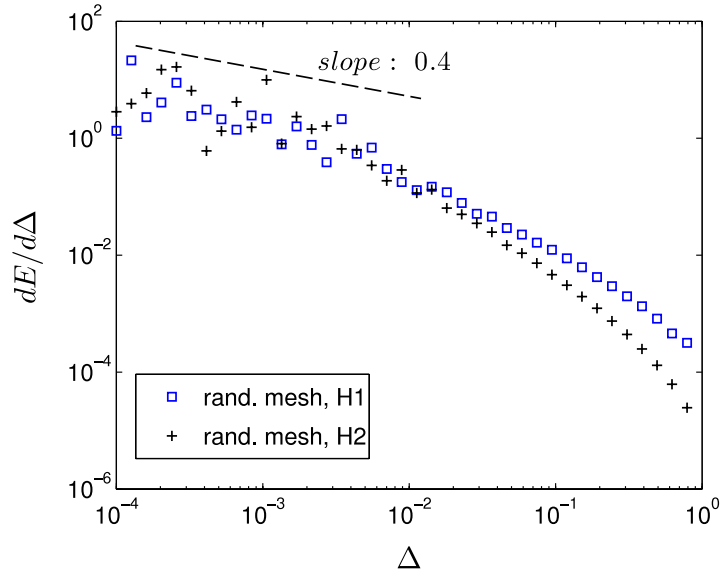

Figure 9. Rate of energy dissipation as a function of the control parameter for the random mesh under strain control, $L = 64$, for H_1- and H_2-ranges of heterogeneity. The slope is given as a guide to support the explanations; it was obtained by fitting a power law to the data for $\Delta < 10^{-2}$.

This introduces an artifact in the estimation of $\langle E \rangle$, and can explain the steep increase of $\mathrm{d}E/\mathrm{d}\Delta$ at the beginning of the simulation, which has therefore no physical significance. In the vicinity of the macroscopic failure, an estimation of the mean dissipated energy $\langle E \rangle$ can be obtained from the probability density function of E, assuming a brutal truncation at E^*:

$$\langle E \rangle_{(\Delta \to 0)} \sim \int_0^{E^*} E^{1-\beta}\, \mathrm{d}E \sim E^{*2-\beta}. \tag{12}$$

Neglecting the finite size effect, we can therefore approximate the evolution of the mean dissipated energy by $\langle E \rangle_{(\Delta \to 0)} \sim \Delta^{-\gamma(2-\beta)}$ (a similar relation was obtained for the average avalanche size for ferromagnets [50]). Typical values of the exponents (table 2) suggest generally a very shallow evolution of $\langle E \rangle$ near the macroscopic failure. For example, considering the random mesh under stress control (H_2-range of heterogeneity), $\gamma_E(2 - \beta_E) \simeq 0.2 \pm 0.7$. This estimation is commensurate with the shallow increase of $\mathrm{d}E/\mathrm{d}\Delta$ near the macroscopic failure (figure 9). For $\Delta < 10^{-2}$ the slope can be roughly approximated as 0.4. However, despite extensive statistical sampling, the power law behavior and the slope expected to characterize the evolution of $\mathrm{d}E/\mathrm{d}\Delta$ in the vicinity of the macroscopic failure cannot be clearly assessed. The range of material heterogeneity does not affect the evolution of $\mathrm{d}E/\mathrm{d}\Delta$. No significant difference was observed between stress and strain control modes.

4. Spatial correlations of damage events

In this section we analyze the spatial distribution of damage using a two-point correlation function. For a population of $\mathcal{N}$ damage events, the correlation integral is defined

J. Stat. Mech. (2010) P01013

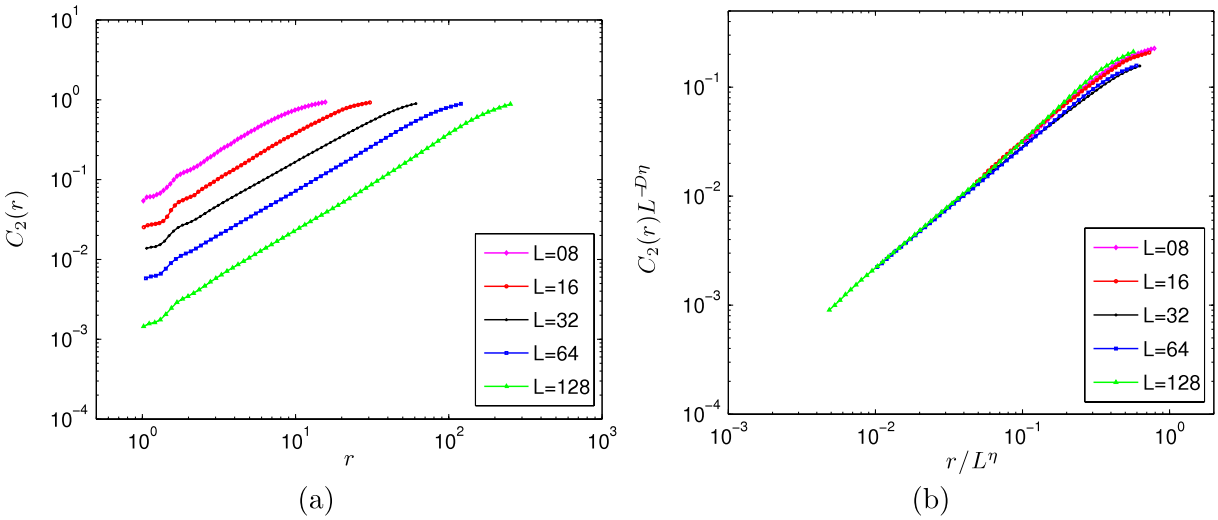

Figure 10. (a) The correlation integral $C_2(r)$ for damage events near peak load ($\Delta < 10^{-2}$) for different system sizes, for the random mesh under strain control (H_1-range). (b) Data collapse analysis of the correlation integrals; the values used for the exponents are $D = 1.15$ and $\eta = 1.1$.

as $C_2(r) = 2\mathcal{N}_p(r)/[\mathcal{N}(\mathcal{N}-1)]$, where $\mathcal{N}_p(r)$ is the number of pairs of points whose separation is less than r [51]. For a fractal population of elements, $C_2(r)$ is expected to scale with r, e.g. as r^D, where D is the correlation dimension of the system. The distance r is expressed in the same units as the system size L.

4.1. Finite size scaling

We first analyze the correlation function in the vicinity of the macroscopic failure ($0 < \Delta < 10^{-2}$). We calculate the correlation integral of damage events corresponding to this criterion and average it over all realizations of the disorder for system sizes $L \geq 8$. The form of the correlation function obtained is a power law with a crossover at large r values (figure 10):

$$C_2(r) \sim r^D \mathcal{F}(r/r_0) \tag{13}$$

where D is the correlation dimension of damage events and the function $\mathcal{F}$ describes the crossover occurring at r_0, so $\mathcal{F}(r/r_0) \sim$ const for $r \ll r_0$ and $\mathcal{F}(r/r_0) \sim r^{-D}$ for $r \gg r_0$. The crossover length r_0 increases with the system size L. We assume that it expresses a finite size effect and scales as $r_0 \sim L^{\eta}$. To test this scaling and estimate the value of η we perform a data collapse (figure 10). The estimated values for the exponents are given in table 2. The values of D and η are not significantly affected by the loading mode or the mesh type. Both values are very close to 1 for the H_1-range of heterogeneity, arguing for a spatial distribution of damage over quasi-linear structures, the faults. On the other hand, the H_2-range leads to slightly larger values of the correlation dimension D (table 3). This suggests that increasing the heterogeneity leads to a more isotropic interaction of damage events and more branched fault geometries (see figure 2).

J. Stat. Mech. (2010) P01013

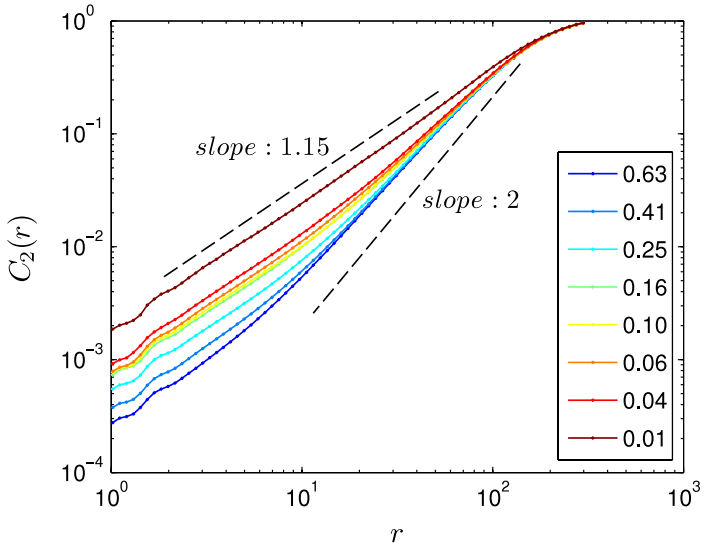

Figure 11. Correlation integrals of damage events for the random mesh under strain control, $L = 128$ (H_1-range), for different values of the control parameter Δ.

4.2. Evolution of the correlation length

We analyze the evolution of spatial correlations of damage with the control parameter Δ. In order to do so, we divide each simulation into intervals containing a similar number of damage events. For each interval, the mean control parameter and the correlation integral corresponding to the population of damage events are calculated. The correlation integrals are sorted into bins of the mean control parameter and averaged over disorder. In the early stages of the simulation, there appear to be two different scaling regimes (figure 11). For small values of r, the correlation integrals scale as r^D. This scaling extends up to a crossover length, which we refer to as the correlation length ξ. Beyond the correlation length, the scaling exponent of integrals rises to 2, which corresponds to a homogeneous unclustered damage pattern. Finally, a second crossover occurs and the integrals bend down due to the finite size scaling described in section 4.1. This evolution is best seen when renormalizing the integrals by the integral closest to the peak load (figure 12). The evolution of spatial correlations of damage can thus be seen as a divergence of the correlation length ξ on approaching $\Delta = 0$:

$$C_2(r, \Delta) \sim r^D \mathcal{G}(r/\xi) \tag{14}$$

where ξ is expected to grow as $\xi \sim \Delta^{-\lambda}$. The function $\mathcal{G}$ describes the first crossover, occurring at ξ, so $\mathcal{G}(r/\xi) \sim$ const for $r \ll \xi$ and $\mathcal{G}(r/\xi) \sim r^{2-D}$ for $r \gg \xi$. The second crossover, due to the FSS, is not accounted for here. We test this hypothesis and estimate the value of λ with a data collapse analysis (figure 13). As the FSS is neglected in equation (14), only the parts of the integrals that are not affected by the FSS can be expected to collapse. A good collapse is obtained for $\lambda = 1.0$ (tables 2 and 3). As for avalanches, the critical exponent λ is found to be similar for the stress and strain loading modes and does not vary significantly with the mesh type or with the heterogeneity.

J. Stat. Mech. (2010) P01013

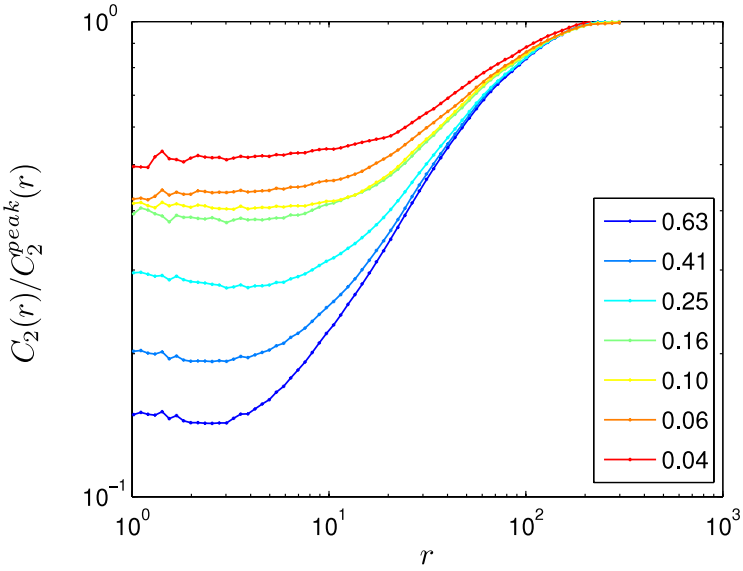

Figure 12. Correlation integrals normalized by the peak load integral (random mesh under strain control, $L = 128$, H_1-range).

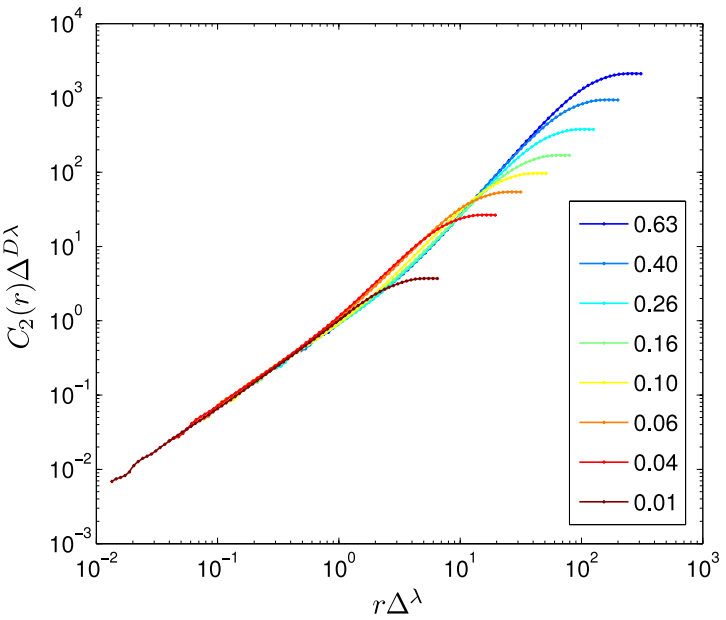

Figure 13. Data collapse analysis of the correlation integral $C_2(r)$ for the random mesh under strain control ($L = 128$, H_1-range). The values used for the exponents are $D = 1.15$ and $\lambda = 1.0$.

Therefore, the correlation length diverges as $1/\Delta$ on approaching the peak load. This value of the critical exponent is slightly smaller than the corresponding value obtained for two-dimensional geometrical percolation (4/3; see e.g. [52]), meaning that the elastic interactions imply a less abrupt divergence of the correlation length near the critical point.

doi:10.1088/1742-5468/2010/01/P01013

J. Stat. Mech. (2010) P01013

5. Spatial dependence of the strain rate field

Strain rates are computed over a broad range of spatial scales for different values of the control parameter Δ through the following procedure. Each simulation is divided into intervals containing a similar number of damage events. We compute the rate of displacement (u, v) as the difference between the displacements at the beginning and the end of each interval. The spatial gradients of the displacement rate (or strain rate tensor components) $\partial u/\partial x$, $\partial v/\partial x$, $\partial u/\partial y$, $\partial v/\partial y$ are calculated. We then consider the invariants of the strain rate tensor:

$$\dot{\epsilon}_{\mathrm{div}} = \frac{\partial u}{\partial x} + \frac{\partial v}{\partial y} \tag{15}$$

$$\dot{\epsilon}_{\mathrm{shear}} = \left[\left(\frac{\partial u}{\partial x} - \frac{\partial v}{\partial y} \right)^2 + \left(\frac{\partial u}{\partial y} + \frac{\partial v}{\partial x} \right)^2 \right]^{1/2} \tag{16}$$

where $\dot{\epsilon}_{\mathrm{div}}$ and $\dot{\epsilon}_{\mathrm{shear}}$ are respectively the divergence and shear rates. Henceforth the term deformation means the quantity $\dot{\epsilon} = \sqrt{\dot{\epsilon}^2_{\mathrm{shear}} + \dot{\epsilon}^2_{\mathrm{div}}}$, also known as the total deformation rate. Deformation at the finite element scale, the smallest scale, is first computed. At larger spatial scales deformation is obtained by a coarse graining procedure. Consider a square box of width W centered at a certain location within the mesh. We find all the element centers that lie inside the box and compute the average displacement rate gradients over all the corresponding elements, where the contribution of each element is weighted by its area. From these large-scale gradients we compute the deformation rates $\dot{\epsilon}$. Assuming scaling isotropy, we define the spatial scale l as the square root of the actual area covered by the elements (which is close to W^2). By changing the size of the box we obtain samples of the deformation at different scales. Deformation is binned with respect to spatial scale and control parameter and averaged over different realizations of the disorder. This procedure can only be applied to large systems ($L \geq 32$) where a wide range of scales can be covered.

In the early stages of the simulation, deformation is homogeneously scattered throughout the system, while near macroscopic failure, it is extremely heterogeneous and localized along linear features (figure 14). The mean total deformation $\langle \dot{\epsilon} \rangle$ is plotted as a function of the spatial scale l and the control parameter Δ (figure 15). $\langle \dot{\epsilon} \rangle$ shows a power law decrease with increasing l up to a given crossover scale:

$$\langle \dot{\epsilon} \rangle (l, \Delta) \sim l^{-\rho} \mathcal{H}(l/l^*), \tag{17}$$

where l^* is the crossover scale that increases on approaching the macroscopic failure. The function $\mathcal{H}$ describes the crossover; it is thus constrained by $\mathcal{H}(l/l^*) \sim$ const for $l \ll l^*$ and $\mathcal{H}(l/l^*) \sim l^{\rho}$ for $l \gg l^*$. In order to investigate the possible influence of a finite size effect on the crossover, we analyzed deformation near peak load ($\Delta \leq 10^{-2}$) for various system sizes. No dependence of the crossover on the system size was found; we are therefore unable to properly characterize a finite size effect. The fact that the finite size effect is not noticeable might be related to the boundary conditions applied to the model, since the lateral boundaries of the model can deform freely.

To test the scaling of equation (17), we thus neglect the finite size effect and hypothesize that l^* grows as $l^* \sim \Delta^{-\nu}$. The exponent values are estimated through a data

J. Stat. Mech. (2010) P01013

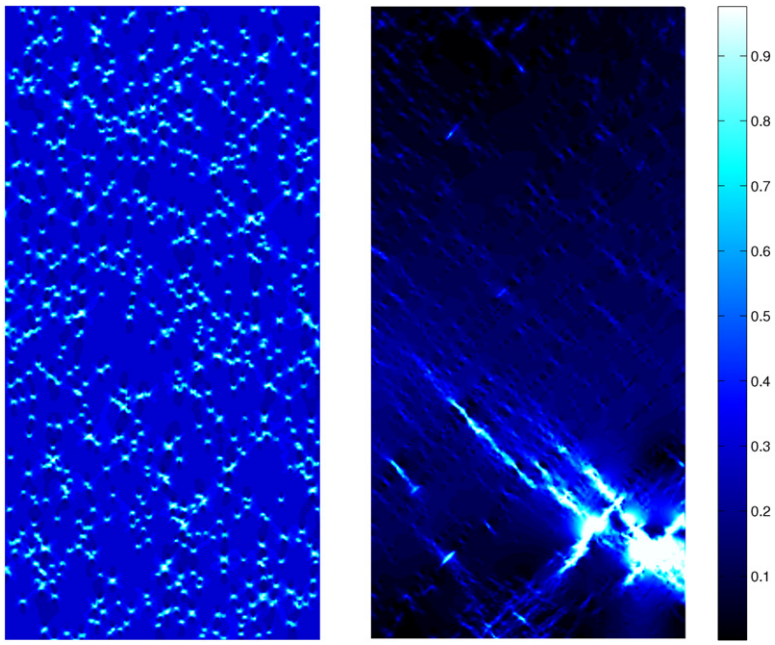

Figure 14. Examples of total deformation rate fields $\dot{\epsilon}$ for $\Delta \simeq 0.9$ (left panel) and $\Delta \simeq 0.01$ (right panel), for the random mesh under strain control (H_1-range, $L = 128$). $\dot{\epsilon}$ is normalized by its maximum value.

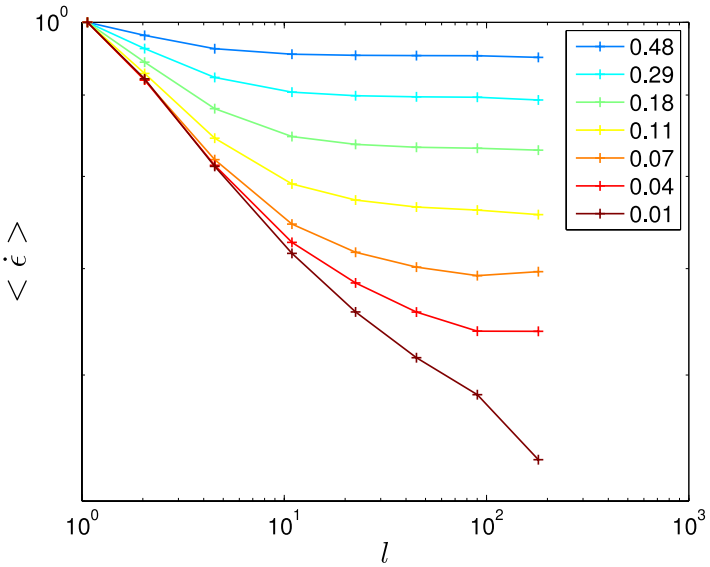

Figure 15. Mean total deformation rate as a function of the spatial scale l and of the control parameter Δ, for the random mesh under strain control (H_1-range, $L = 128$). Deformation rates are normalized at scale $l = 1$.

collapse analysis (figure 16). $\rho = 0.15 \pm 0.02$ and $\nu = 1.0 \pm 0.1$ allow the best collapse independently of the loading mode, the mesh type or the range of material heterogeneity (tables 2 and 3). Small deviations of the data collapse are found in the vicinity of the final failure. These deviations might be due to a finite size effect which was neglected.

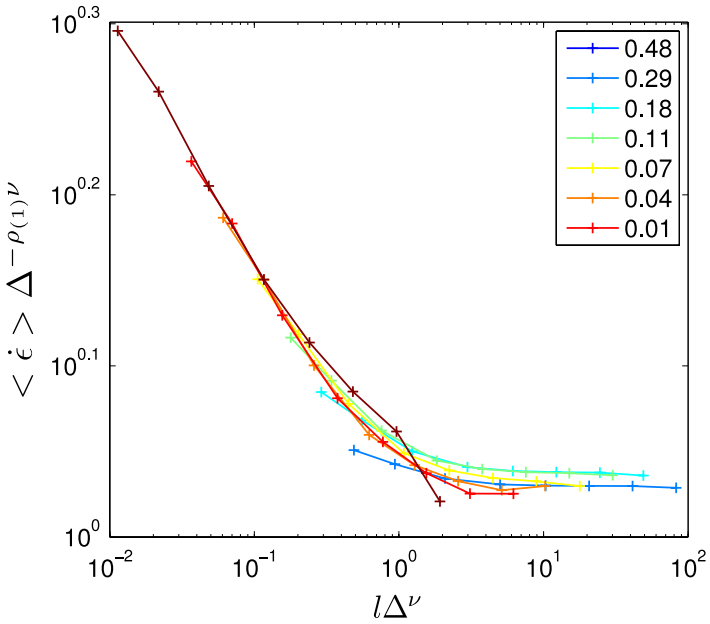

Figure 16. Data collapse analysis of the mean total deformation rate for the random mesh under strain control (H_1-range, $L = 128$). The values used for the exponents are $\rho = 0.15$ and $\nu = 1.0$.

The striking agreement between the values of λ and ν argues for the interpretation of l^* as a correlation length, $l^* \sim \xi$. This results bridges between the two different ways of analyzing the deformation resulting from damage and fracturing, from the discrete approach (through correlation analysis of individual events) to the continuous one (the scaling analysis of the resulting strain field).

As was done for an analysis of Arctic sea ice deformation [35], the scale-dependent heterogeneity of deformation is examined more thoroughly by use of a multifractal analysis which characterizes the scaling of the moments $\langle \dot{\epsilon}^q \rangle$ for $0 < q < 3$. This moment analysis is a way to investigate the scale dependence of the entire distribution of $\dot{\epsilon}$. Generalizing equation (17), we estimate the scaling exponents $\rho(q)$ and the critical exponents $\nu(q)$ by data collapse analysis (figure 17). $\nu = 1$ is found to be constant, independently of the moment order, as one would expect for a correlation length, while $\rho(q)$ shows a curvature indicating the multifractality of the deformation (figure 18). The multifractality is a well-known property of turbulent flow of fluids (e.g. [53]). It is observed here to also arise from long-range elastic interactions in a deforming solid. This means that deformation becomes more and more localized as one decreases the scale of observation.

6. Discussion

6.1. Failure as a critical phenomenon

As noted in section 1, the interpretation of failure as a critical phenomenon [3] is still partly controversial [2, 20]. Following on from discrete statistical models of fracture, such as the RFM, our continuum progressive damage model argues for such a critical point interpretation of failure. The advantage of the present model based on a continuum

J. Stat. Mech. (2010) P01013

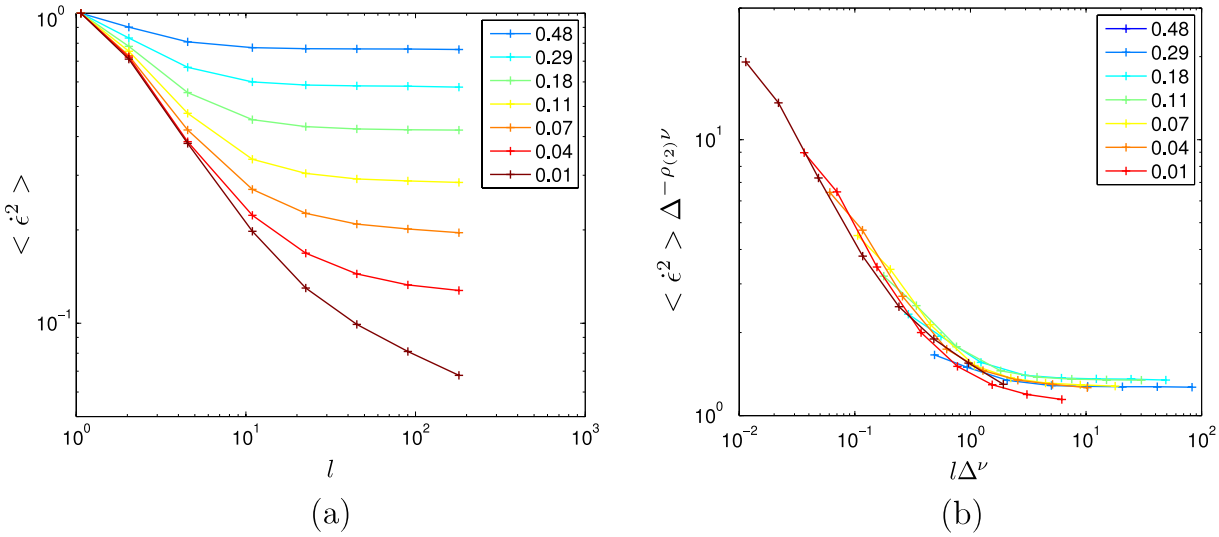

Figure 17. (a) Second moment of deformation $\langle \epsilon^2 \rangle$ as a function of the spatial scale l and of the control parameter Δ. (b) The second moment can be collapsed with the exponents $\rho = 0.65$, $\nu = 1.0$ (random mesh under strain control, H_1-range, $L = 128$).

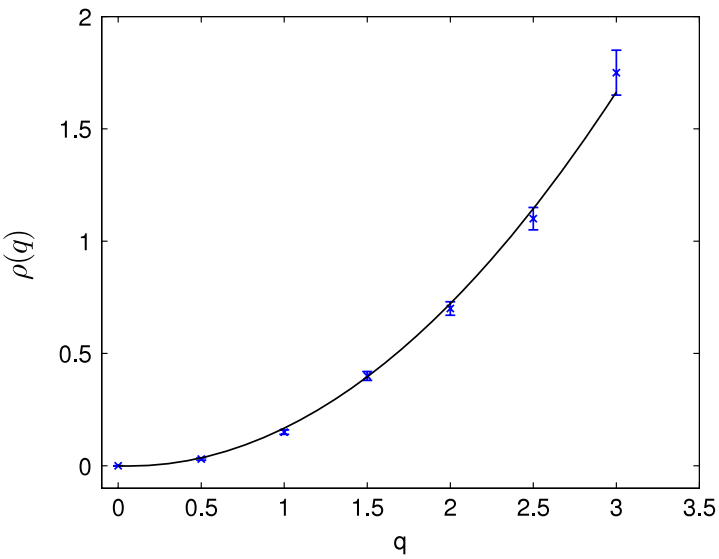

Figure 18. The function $\rho(q)$ versus moment order q (random mesh under strain control, H_1-range, $L = 128$). The exponents $\rho(q)$ are determined by data collapse analysis. The black line is a quadratic fit of $\rho(q) = aq^2 + bq$ where $a = 0.19$ and $b = -0.026$.

mechanics framework is the possibility of tracking criticality from the evolution of the strain field. In terms of damage avalanches, power law distributions of avalanche sizes and energies are observed, associated with a finite size scaling. This finite size scaling, which is also observed for the spatial correlations of the damage events, argues for this critical point interpretation.

J. Stat. Mech. (2010) P01013

Another strong argument is the divergence of the correlation length on approaching macroscopic failure, $\xi \sim 1/\Delta$, which can be seen from a correlation analysis of discrete events (section 4.2) or from a scaling analysis of the continuous strain rate field (section 5). Qualitatively, this is also in agreement with the divergence of the avalanche cut-off (section 3.2). However, one would expect this correlation length to be related to the avalanche cut-off size through the geometrical relation $S^* \sim \xi^D$. This is not really consistent with the value found for the critical exponent γ_S as it yields $\xi \sim \Delta^{-\gamma_S/\delta_S}$, with $\gamma_S/D = 1.7$ for the H_1-range, significantly larger than $\lambda = \nu = 1.0$. This comparison slightly improves for the H_2-range. This divergence of the correlation length can be interpreted as follows. At the early stages of deformation, when the spatial distribution of damage is imposed by the disorder, events are spread uniformly throughout the medium and are uncorrelated. On approaching the macroscopic failure (the critical point), i.e. on decreasing Δ, damage clusters appear as a result of elastic interactions, associated with a correlation length ξ. Within these clusters, damage is organized following a fractal pattern characterized by a fractal dimension D, which is independent of Δ, whereas there is no correlation between clusters. This means that damage and deformation can be homogenized for scales significantly larger than ξ, as shown by the scaling analysis of the strain rate (figure 15). Consequently, homogenization is impossible at the critical point, as no characteristic scale can be defined.

An analysis of cluster size evolution was performed to complement this interpretation. We define the cluster size C_S as the number of adjacent elements (i.e. elements with two common nodes) encountering one or more damage events over a given bin of Δ. The distribution function of cluster sizes follows a power law with an exponential cut-off at large sizes that diverges on approaching peak load:

$$P(C_S) \sim {C_S}^{-\Gamma} \exp(-C_S/C_S^*). \tag{18}$$

For example, with the random mesh ($L = 128$) under strain control and H_1-range of heterogeneity, we find $\Gamma = 1.8 \pm 0.1$ and $C_S^* \sim \Delta^{-\Theta}$ with $\Theta = 0.9 \pm 0.1$ by data collapse analysis. As the surface area of clusters is proportional to their size C_S, we obtain the geometrical relation $C_S^* \sim \xi^D$. In terms of exponents, this relation reads $\Theta = \lambda D$, which is approximately commensurate with the exponent values. Moreover, we verified that cluster barycenters are not spatially correlated: the associated correlation dimension is close to 2, except in the vicinity of macroscopic failure where it slightly decreases due to the finite size effect.

This interpretation, based on the divergence of the correlation length, differs from those of previous studies, which proposed instead a decrease of the correlation dimension of damage patterns on approaching final failure [19, 25, 27]. Similarly, it has been argued that a decrease of the power law exponent β of the avalanche sizes or energies could be a precursory phenomenon of failure [8]. From our results and previous work [23], we argue instead for a β value independent of Δ but a diverging cut-off. For poorly statistically constrained distributions, this can lead to an artificial decrease of the 'apparent' power law exponent, a point raised by Amitrano *et al* [8].

On approaching the critical point, the damage cluster length approaches the system size, and finite size scaling ensues. The close agreement between the values of the finite size exponents δ_S and η, and the correlation dimension D is in agreement with the fact that damage avalanches (faults) are characterized by the same fractal structure whatever

J. Stat. Mech. (2010) P01013

their size, proximity to final failure, or size of the system. Finally, we stress that none of the exponents shows significant variation with the type of mesh or the loading mode, considering the level of uncertainty. Regarding the influence of the loading mode, our results contradict some of the conclusions of Guarino *et al* [13]. Changing the range of material heterogeneity slightly affected the value of the correlation dimension D but it did not have a significant effect on the other exponents.

6.2. Criticality of fracture and deformation of geophysical objects, and precursory phenomena

The scaling properties characterizing damage and deformation near the critical point resemble those reported for the deformation and fracturing of geophysical objects such as the Earth's crust or the sea ice cover. The possible critical character of Earth's crust deformation and fracturing is a long-standing problem (e.g. [54]), and still an active field of research. A thorough review of this problem is beyond the scope of this paper. In the light of the results presented in previous sections, we discuss here only several specific aspects.

The power law distribution of earthquake sizes or energies is well known [31], generally without cut-off, although truncated distributions have been reported [55], and interpreted as a sub-critical state of the crust at a regional scale (e.g. [56]). Fractal clustering of hypocenters has been reported from correlation analyses similar to that discussed in section 4 [32, 33], however without a crossover scale as shown in figure 11. The strain localization of the Arctic sea ice cover, characterized from a continuous approach (strain rate fields), closely resembles the behavior detailed in section 5 near the critical point: the mean total strain rate scales as $\langle \dot{\epsilon} \rangle \sim l^{-\rho}$ with $\rho = 0.20 \pm 0.05$, and is associated with a multifractal scaling [35, 57]. At the timescale of the analysis (three days), no cut-off scale was detected.

The agreement between the scaling properties of the present model near the critical point and those associated with the deformation and fracturing of geophysical objects, as well as the absence of obvious cut-off or crossover scales in this latter case, suggest that these objects remain most of the time near criticality, in a 'marginally stable state' [56]. However, as stressed in the introduction, attempts have been made to export the critical point concept and the associated precursory phenomena to crustal deformation in order to predict 'large' earthquakes. The underlying hypothesis is that, instead of remaining near criticality, crustal deformation is characterized at the regional scale by successive 'large' earthquakes (failures), each of them being considered as a critical point with associated precursory phenomena. These large earthquakes are assumed to release the stresses in their surrounding region, moving it away from criticality until tectonic loading progressively re-establishes the route towards the next critical point [39]. One difficulty with such approaches is the definition of the appropriate space and time windows over which the analysis should be performed, and what 'large' earthquake means as the system never falls apart.

The critical behavior of the model presented in this study is not affected by the loading mode, as long as the control parameter is correctly defined. In the case of geophysical objects, the loading conditions may be hard to identify and depend on the situation. Cliff collapses or landslides are driven by constant stress loadings, while for volcanoes

J. Stat. Mech. (2010) P01013

the pressure increase in the magma chamber causes the stress to increase. Regarding geological faults, the loading is generally a complex mixture between strain and stress depending on the tectonic conditions, strain being the only parameter reachable via field measurements. In such cases the control parameter is usually from a timescale.

The most discussed precursory phenomenon is a divergence of the so-called Benioff strain ϵ_{B} on approaching a large earthquake [28, 37, 39, 40]:

$$\epsilon_{\mathrm{B}}(t) = \sum_{i=1}^{N(t)} \sqrt{E_i(t)} = A - B(t_{\mathrm{c}} - t)^m \tag{19}$$

where E_i is the seismic energy of the ith event, $N(t)$ the cumulative number of events since an initial time (to be defined), t_{c} the arrival time of the large earthquake, $A = \epsilon_{\mathrm{B}}(t = t_{\mathrm{c}})$, $B = A/{t_{\mathrm{c}}}^m$, and m a critical exponent generally considered to be close to 0.3. Recast in terms of strain rate and control parameter $\Delta = (t_{\mathrm{c}} - t)/t_{\mathrm{c}}$, this reads $\mathrm{d}\epsilon_{\mathrm{B}}/\mathrm{d}\Delta \sim \Delta^{m-1} \approx \Delta^{-0.7}$. This increase of the Benioff strain rate (or of the energy release rate) before the critical point can result from (i) an increase of the earthquake occurrence rate and/or (ii) from an increase of the mean energy $\langle E \rangle$, as in section 3.3. Analyzing regional seismicity before several large earthquakes in California and Alaska, Jaume and Sykes [39] argued that factor (i) is generally not observed, whereas factor (ii) is more likely and is associated with a diverging cut-off size (or energy) on approaching the large earthquake. Using a methodology similar to that detailed in section 3.3, a possible link between a diverging cut-off strain ϵ_{B}^* (or energy E^*) and a diverging Benioff strain rate can be discussed. If the earthquake occurrence rate remains constant, we have

$$\frac{\mathrm{d}\epsilon_{\mathrm{B}}}{\mathrm{d}t}_{(\Delta \to 0)} \sim \langle E^{1/2} \rangle_{(\Delta \to 0)} \sim \int_0^{E^*} P(E) E^{1/2}\, \mathrm{d}E \sim {E^*}^{(3/2)-\beta} \sim {\epsilon_{\mathrm{B}}^*}^{3-2\beta}, \tag{20}$$

the above integral being only defined if the power law exponent of the seismic energy $\beta < 3/2$. In such a case, equation (20) would lead to the scaling relation $\mathrm{d}\epsilon_{\mathrm{B}}/\mathrm{d}\Delta \sim \Delta^{-(\gamma/2)(3-2\beta)}$. For $\beta > 3/2$, the integral of equation (20) is no longer defined. In this case the Benioff strain rate is controlled by the smallest earthquakes and by a lower cut-off in the distribution of seismic energy. A b-value (power law exponent of the cumulative distribution of earthquake magnitudes) around 1, as generally reported, yields $\beta \approx 5/3$ [58]. This means that the evolution of the Benioff strain rate towards $\Delta = 0$ is either extremely shallow, or very difficult to estimate. This might explain why a possible divergence of the Benioff strain rate before large earthquakes remains highly controversial [40].

Zoller *et al* [38] have proposed another precursor phenomenon, the divergence of the correlation length ξ. To estimate ξ from a seismic catalog, they did not perform a correlation analysis such as the one described in section 4, but instead used a more complex iterative procedure, the single-link cluster analysis [59]. They claimed that at least some large Californian earthquakes were preceded by a divergence of ξ, with an exponent λ varying from 0.24 to 0.57, i.e. a divergence much less abrupt than the one observed with the present model ($\lambda = 1$). However, within a critical point framework, critical exponents should be robust and not vary from one case to another.

In conclusion, although the scaling laws describing the deformation of geophysical objects share obvious features with what is observed near the critical point in statistical

J. Stat. Mech. (2010) P01013

models of fracture (including the present one), we wonder to what extent such models based on irreversible damage are relevant for crustal or sea ice deformation. One important lacking ingredient is, we believe, the presence of recovery (healing) mechanisms that would compensate for increasing damage.

Acknowledgments

All (or most of) the computations presented in this paper were performed at the Service Commun de Calcul Intensif de l'Observatoire de Grenoble (SCCI-CIMENT). L Girard is supported by a BDI PhD grant from CNRS. D Amitrano thanks the French program INSU-Catell and the EU program Trigs for support.

References

[1] Griffith A A, 1920 *Phil. Trans. R. Soc.* A **221** 163
[2] Alava M J, Nukala P and Zapperi S, 2006 *Adv. Phys.* **55** 349
[3] Sornette D and Andersen J V, 1998 *Eur. Phys. J.* B **1** 353
[4] Weibull W, 1939 *Proc. R. Swed. Acad. Eng. Sci.* **151** 5–45
[5] Sethna J P, Dahmen K A and Myers C R, 2001 *Nature* **410** 242
[6] Deschanel S, Vanel L, Godin N, Vigier G and Ciliberto S, 2009 *J. Stat. Mech.* P01018
[7] Amitrano D, 2003 *J. Geophys. Res.* **108** 2044
[8] Amitrano D, Grasso J R and Senfaute G, 2005 *Geophys. Res. Lett.* **32** L08314
[9] Salminen L I, Tolvanen A I and Alava M J, 2002 *Phys. Rev. Lett.* **89** 185503
[10] Petri A, Paparo G, Vespignani A, Alippi A and Costantini M, 1994 *Phys. Rev. Lett.* **73** 3423
[11] Scholz C H, 1968 *Bull. Seismol. Soc. Am.* **58** 399
[12] Smith W D, 1981 *Nature* **289** 136–9
[13] Guarino A, Garcimartin A and Ciliberto S, 1998 *Eur. Phys. J.* B **6** 13
[14] Nechad H, Helmstetter A, Guerjouma R E and Sornette D, 2005 *Phys. Rev. Lett.* **94** 045501
[15] Amitrano D and Helmstetter A, 2006 *J. Geophys. Res.* **111** B11201
[16] Lockner D, 1993 *Int. J. Rock Mech. Min. Sci. Geomech. Abstr.* **30** 883
[17] Lockner D A, Byerlee J D, Kuskenko V, Ponomarev A and Sidorin A, 1991 *Nature* **350** 39
[18] Lockner D A and Byerlee J D, 1991 *Vth Conf. AE/MS Geol. Str. and Mat.* ed Hardy (Trans Tech Publications, The Pennsylvania State University) p 45
[19] Hirata T, Satoh T and Ito K, 1987 *Geophys. J. R. Astron. Soc.* **90** 369
[20] Picallo C B and Lopez J M, 2008 *Phys. Rev.* E **77** 046114
[21] Hemmer P C and Hansen A, 1992 *J. Appl. Mech.* **59** 909
[22] Herrmann H J and Roux S, 1990 *Statistical Models for the Fracture of Disordered Media* (Amsterdam: North-Holland)
[23] Zapperi S, Nukala P K V V and Simunovic S, 2005 *Phys. Rev.* E **71** 026106
[24] Pradhan S, Hansen A and Hemmer P, 2005 *Phys. Rev. Lett.* **95** 125501
[25] Cowie P A, Sornette D and Vanneste C, 1995 *Geophys. J. Int.* **122** 457
[26] Amitrano D, Grasso J R and Hantz D, 1999 *Geophys. Res. Lett.* **26** 2109
[27] Amitrano D, 2006 *Int. J. Fract.* **139** 369
[28] Bowman D D, Ouillon G, Sammis C G, Sornette A and Sornette D, 1998 *J. Geophys. Res.* **103** 24359
[29] Pradhan S, Hansen A and Hemmer P C, 2009 *IUTAM Symposium on Scaling in Solid Mechanics* ed F M Borodich (Berlin: Springer) chapter (Burst Statistics as a Criterion for Imminent Failure) p 165
[30] Grasso J R and Sornette D, 1998 *J. Geophys. Res.* **103** 29965
[31] Gutenberg B and Richter C, 1954 *Seismicity of the Earth and Associated Phenomenon* (Princeton, NJ: Princeton University Press)
[32] Kagan Y Y, 2007 *Geophys. J. Int.* **168** 1175
[33] Kagan Y Y and Knopoff L, 1980 *Geophys. J. R. Astron. Soc.* **62** 303
[34] Weiss J, 2003 *Surv. Geophys.* **24** 185
[35] Marsan D, Stern H, Lindsay R and Weiss J, 2004 *Phys. Rev. Lett.* **93** 178501
[36] Weiss J, Marsan D and Rampal P, 2009 *IUTAM Symposium on Scaling in Solid Mechanics* ed F M Borodich (Berlin: Springer) chapter (Space and Time Scaling Laws Induced by the Multiscale Fracturing of the Arctic Sea Ice Cover) p 101

J. Stat. Mech. (2010) P01013

[37] Bufe C G and Varnes D J, 1993 *J. Geophys. Res.* **98** 9871
[38] Zoller G, Hainzl S and Kurths J, 2001 *J. Geophys. Res.* **106** 2167
[39] Jaume S and Sykes L, 1999 *Pure Appl. Geophys.* **155** 279
[40] Hardebeck J L, Felzer K R and Michael A J, 2008 *J. Geophys. Res.* **113** B08310
[41] Kachanov M, 1994 *Adv. Appl. Mech.* **30** 259
[42] Katz O and Reches Z, 2004 *J. Geophys. Res.* **109** B01206
[43] Amitrano D and Schmittbuhl J, 2002 *J. Geophys. Res.* **107** 2375
[44] Jaeger J C and Cook N G W, 1983 *Fundamentals of Rock Mechanics* (London: Chapman and Hall)
[45] Zapperi S, Vespignani A and Stanley E, 1997 *Nature* **388** 658
[46] Byerlee J D, 1978 *Pure Appl. Geophys.* **116** 615–26
[47] Weiss J and Schulson E M, 2009 *J. Phys. D: Appl. Phys.* **42** 214017
[48] Evans A G, *Acoustic emission sources in brittle solids*, 1979 *Fundamentals of Acoustic Emission* ed K Ono (Los Angeles, CA: University of California)
[49] Chessa A, Vespignani A and Zapperi S, 1999 *Comput. Phys. Commun.* **121** 299
[50] Zapperi S, Cizeau P, Durin G and Stanley H E, 1998 *Phys. Rev.* B **58** 6353
[51] Hentschel H G E and Proccacia I, 1984 *Physica* D **8** 435
[52] Stauffer D and Aharony A, 1994 *Introduction to Percolation Theory* (London: Taylor and Francis)
[53] Frisch U, 1995 *Turbulence: The Legacy of A N Kolmogorov* (Cambridge: Cambridge University Press)
[54] Sornette A and Sornette D, 1989 *Europhys. Lett.* **9** 197
[55] Burroughs S M and Tebbens S F, 2002 *Bull. Seismol. Soc. Am.* **92** 2983
[56] Main I, 1996 *Rev. Geophys.* **34** 433
[57] Stern H L and Lindsay R W, 2009 *J. Geophys. Res.* **114** C10017
[58] Kanamori H, 1978 *Nature* **271** 411
[59] Frohlich C and Davis S D, 1990 *Geophys. J. Int.* **100** 19

J. Stat. Mech. (2010) P01013